Letter Vol. 47, No. 13 / 1 July 2022 / Optics Letters 3171

Optics Letters

Sensitive and single-shot OH and temperature measurements by femtosecond cavity-enhanced absorption spectroscopy

NING LIU,[1,*] HONGTAO ZHONG,[1] TIMOTHY Y. CHEN,[1,2] YING LIN,[1] ZIYU WANG,[1] AND YIGUANG JU[1]

[1] Department of Mechanical and Aerospace Engineering, Princeton University, Princeton, NJ 08544, USA
[2] Presently at Sandia National Laboratories, Livermore, CA 94550, USA
*Corresponding email: nl7@princeton.edu

Received 8 April 2022; revised 23 May 2022; accepted 31 May 2022; posted 31 May 2022; published 22 June 2022

In many low-temperature plasmas (LTPs), the OH radical and temperature represent key properties of plasma reactivity. However, OH and temperature measurements in weakly ionized LTPs are challenging, due to the low concentration and short lifetime of OH and the abrupt temperature rise caused by fast gas heating. To address such issues, this Letter combined cavity-enhanced absorption spectroscopy (CEAS) with femtosecond (fs) pulses to enable sensitive single-shot broadband measurements of OH and temperature with a time resolution of ~180 ns in LTPs. Such a combination leveraged several benefits. With the appropriately designed cavity, an absorption gain of ~66 was achieved, enhancing the actual OH detection limit by ~55× to the 10^{11} cm^{-3} level (sub-ppm in this work) compared with single-pass absorption. Single-shot measurements were enabled while maintaining a time resolution of ~180 ns, sufficiently short for detecting OH with a lifetime of ~100 μs. With the broadband fs laser, ~34,000 cavity modes were matched with ~95 modes matched on each CCD pixel bandwidth, such that fs-CEAS became immune to the laser-cavity coupling noise and highly robust across the entire spectral range. Also, the broadband fs laser allowed simultaneous sensing of many absorption features to enable simultaneous multi-parameter measurements with enhanced accuracies.

https://doi.org/10.1364/OL.460338

Non-equilibrium low-temperature plasmas (LTPs) have been widely applied across many fields, including fuel reforming [1], pollution reduction [2], and surface treatment [3], since LTPs are energy efficient and use electrical energy to generate energetic electrons and reactive species rather than to heat the gas. In LTPs, the hydroxyl (OH) radical and temperature represent key properties of plasma chemistry, and their measurements are of fundamental importance. However, simultaneous measurements of OH and temperature in weakly ionized LTPs are challenging for two reasons: first, the relatively low OH concentration (typically at $\sim10^{12}$ cm^{-3} or lower [4]) often lies beyond the detection limits of most previous diagnostics; second, the short lifetime of OH, typically ranging from ~10 μs to ~100 μs, necessitates measurements with sub-μs time resolution. In parallel, temperature measurements in LTPs also face a similar challenge in time resolution. The fast gas heating mechanism in LTPs leads to an abrupt gas temperature rise, e.g., a 1000-K rise within ~10 μs to ~10 ns [5], requiring sub-μs to sub-ns time resolution. Therefore, there is strong motivation to enable sensitive single-shot simultaneous OH and temperature measurements with sufficiently short time resolution.

To address the above issue, this Letter reports a diagnostic combining cavity-enhanced absorption spectroscopy (CEAS) with a femtosecond (fs) laser to enable sensitive and single-shot OH and temperature measurements in LTPs with adequate time resolution and accuracy. Such a combination can leverage the advantages from both sides. From the CEAS side, two advantages can be exploited to enhance fs laser absorption. By appropriately designing the cavity, the enhanced OH detection sensitivity and single-shot measurements were allowed while equipped with a ~180 nanoseconds (ns) time resolution. Based on absorption, CEAS enhances the detection sensitivity by increasing the absorption length by tens to hundreds of times using a pair of high-reflectivity mirrors. However, the detection sensitivity determined by the absorption length is fundamentally at odds with the time resolution that depends on the laser pulse time of flight along the absorption length. When the absorption length increases, the sensitivity rises while the time resolution is degraded. This work designed a CEAS to balance sensitivity and time resolution, and this CEAS can detect low-concentration OH *in situ* in LTPs and enable single-shot measurements while maintaining a 180-ns time resolution that is sufficiently short compared with the OH lifetime.

In parallel, two other advantages from the fs laser side can be exploited to improve CEAS: the immunity to laser-cavity coupling noise and multi-parameter (and/or multi-species) measurements with improved accuracies. Currently, the commercial fs lasers have a bandwidth of tens to hundreds cm^{-1} [6,7]. Such broadband nature of fs lasers can enable a total of tens of thousands of longitudinal cavity modes and each CCD pixel bandwidth can match ~100 modes for typical lab-scale cavity cells. Due to this benefit, the cavity across the whole spectral range will become highly immune to the laser-cavity

0146-9592/22/133171-04 Journal © 2022 Optica Publishing Group

Corrected 24 June 2022

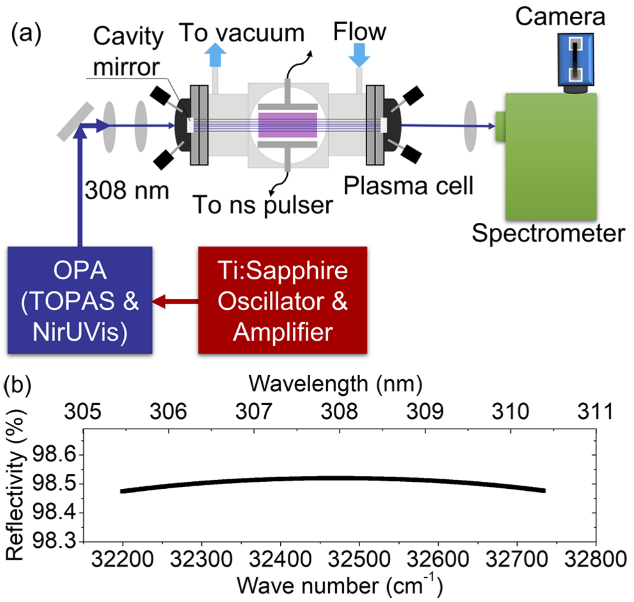

Fig. 1. (a) Experimental setup for fs-CEAS; (b) Reflectivity curve of cavity mirrors.

coupling noise without applying any laser frequency stabilization techniques. In contrast, many past CEAS or cavity ringdown spectroscopy (CRDS) techniques with limited cavity modes (e.g., single-mode CEAS/CRDS [8,9]) needed to stabilize the laser frequency using an extra locking scheme (e.g., the Pound–Drever–Hall scheme [10]), otherwise they would suffer off-mode interferences. Meanwhile, the broadband of fs lasers can be used to enable multi-parameter/species measurements [6,11,12] with enhanced accuracies. With the broadband pulse, a series of OH absorption features can be simultaneously measured. These features will provide abundant constraints to the fit, such that both OH and temperature can be inferred with reduced uncertainties (e.g., due to line overlaps with interfering species)

With the above understanding, we developed the fs-CEAS technique for sensitive, single-shot, simultaneous and *in situ* measurements of OH concentration and temperature with a ~180 ns time resolution. The measurements were demonstrated based on the $X^2\Pi$-$A^2\Sigma^+$ absorption band of OH near 308 nm in UV generated in LTPs, since the OH $X^2\Pi$-$A^2\Sigma^+$ band has marginal interference from other species. Figure 1(a) shows the fs-CEAS setup consisting of a fs laser, a plasma reactor bounded with cavity mirrors, a spectrometer, and a camera. The UV fs laser pulses were generated by a fs laser system (Coherent Astrella). In this laser system, a Ti:Sapphire oscillator and an ultrafast amplifier produced laser pulses centered at 800 nm with 80 fs duration at 1 kHz repetition rate. An optical parametric amplifier (Light Conversion TOPAS NirUVIS) then converted the pulses into the UV pulses centered at 307.8 nm with ~3.2 nm bandwidth and 45 µJ pulse energy.

The fs UV laser pulses were then coupled into a plasma cell bounded with a pair of cavity mirrors in an on-axis configuration. The plasma cell was largely similar to that introduced in Ref. [13] with one difference on the electrodes. Two short cylindrical electrodes separated by 5.5 mm were fixed in parallel in the cell center. The electrodes were made of stainless steel, and one of them was covered by 1.6-mm-thick dielectric quartz. Each electrode had a diameter of 30 mm (absorption path length per pass) with smoothed edges to avoid concentrating electric field. The electrodes were connected to a ns discharge pulser (FID GmbH FPG 30-50MC4) that operated in burst mode with a burst rate of 1 Hz that flushed the plasma volume with new gas between two sequential bursts. Each burst had 600 pulses at a repetition rate of 30 kHz, and each pulse had a duration of 12 ns and a peak voltage of 5 kilovolts.

The left and right parts of the plasma cell were a pair of high-finesse cavity mirrors (Rocky Mountain Inc.) separated by a distance of 0.5 m, and each mirror had a radius of curvature of 6 m and a diameter of 20.3 mm. The reflectivity curve of cavity mirrors as a function of wavelength is shown in Fig. 1(b). This curve was calibrated using a method described in Ref. [14] as summarized in the Supplementary material. As seen, the cavity mirrors featured a reflectivity of ~98.5% near 307.8 nm. This cavity design exhibited two benefits: first, it considerably enhanced the sensitivity for detecting OH by ~66× and allowed single-shot measurements, as opposed to single-pass absorption; second, it also retained a ~180 ns time resolution (determined by cavity ringdown time), which was short enough for detecting transient OH radicals in plasmas. Then, the laser pulses were coupled into this optical cavity at a time instant 300 ns after the target discharge pulse. Here the fs laser's 3.2-nm bandwidth centered at 307.8 nm matched ~34,000 cavity modes with a spectral spacing of 0.01 cm^{-1}, and each camera CCD pixel (as to be mentioned) simultaneously matched ~95 modes, considerably more than those enabled by ns lasers [15]. This mode-matching reduced the laser-cavity coupling noise to 10% or less across the entire spectral range, making the fs-CEAS noise limited by the inevitable laser intensity fluctuations. Therefore, the fs laser significantly stabilized the cavity and immunized the cavity against laser-cavity coupling noise, compared with ns lasers.

Then, the gas mixture flowed into the plasma cell continuously and reacted between two electrodes before being exhausted to vacuum. Two gas mixtures were used. The first mixture involved Helium (He) with a flow rate of 900 sccm (standard cubic centimeter per minute) saturated with water (H_2O) vapor at 100 Torr. The water vapor seeding was achieved by flowing He through a water vessel at ~308 K using a heater. The second mixture involved methane (CH_4), oxygen (O_2) and He of 100, 200, and 640 sccm, respectively, at 90 Torr. Under these conditions, a steady plasma was produced with spatially uniform OH radicals. The OH uniformity was confirmed by instantaneously imaging OH* chemiluminescence, which had an overall relative standard deviation of 2.5%.

Lastly, the laser pulses were taken by a spectrometer and an ICCD camera. Specifically, the laser pulses were focused by a plano–convex lens ($f = 200$ mm) onto the slit (of 50 µm width) of the spectrometer (Acton SP2500i). The spectrometer with a 2400-grooves/mm diffraction grating was used to spectrally disperse the pulses, which were then captured by the camera (Princeton Instruments PIMAX-4 1024i) with a gate time of 1 µs. The camera was synchronized with the fs laser and ns discharge pulser by a delay generator (SRS DG645). Each pixel on the camera chip along the horizontal direction corresponded to a width of 0.96 cm^{-1}. The pixels were vertically binned to improve the signal-to-noise ratio (SNR). The baseline and transmitted laser intensity spectra $I_0(v)$ and $I_t(v)$ along with background noises were captured with the plasma off and on, respectively.

Next, the measured $I_0(v)$ and $I_t(v)$ corrected by background noise were processed by a spectral fitting method to infer the final temperature and OH concentration. This spectral fitting method, similar to those in Refs. [6,16,17], inferred temperature and OH by fitting the calculated fs-CEAS absorbance spectrum to the measured absorbance in five steps. In the first step, temperature and OH concentration were initialized to calculate the fs-CEAS absorbance spectrum based on Eq. (1),

$$\alpha_{CEAS}(\nu) = -\ln\left(\frac{(1-R(\nu)^2)e^{-\alpha_{sp}(\nu)}}{1-R(\nu)^2 e^{-2\alpha_{sp}(\nu)}}\right) \tag{1}$$

where $\alpha_{\text{CEAS}}(\nu)$ denotes the fs-CEAS absorbance at a given wave number ν, $R(\nu)$ the reflectivity of cavity mirrors, and $\alpha_{sp}(\nu)$ the single-pass absorbance obtained using the Beer–Lambert law and the HITRAN database. In $\alpha_{sp}(\nu)$, pressure broadening was unknown (in addition to temperature and OH) to be fitted. Here the OH(X) in LTPs under 400 K (as to be shown later) was in the vibration-rotation equilibrium with negligible population at higher vibrational levels [18], and therefore the equilibrium-based HITRAN database can be applied to OH(X) measurements. In the second step, the measured $I_0(\nu)$ was up-sampled with a high spectral resolution of 0.0002 cm^{-1}, and then combined with $\alpha_{\text{CEAS}}(\nu)$ obtained in step 1 to generate $I_{t,c}(\nu)$. In the third step, the instrument response function (IRF) of the spectrometer-camera system was convolved with $I_{t,c}(\nu)$ to generate instrument broadened $I_{t,c}(\nu)$. The IRF was modelled as a Voigt profile with full width at half maximum as the resolution (i.e., 3.78 cm^{-1}, theoretically computed based on grating dispersion and experimentally verified using a Mercury lamp) of the spectrometer-camera system and with the relative weight between the Gaussian and Lorentzian components to be fitted. In the fourth step, the high-resolution instrument broadened $I_{t,c}(\nu)$ was down-sampled based on cavity modes spaced by 0.01 cm^{-1}, and was then down-sampled (i.e., bin-averaged to reflect the averaging process on each pixel [11]) again based on the camera pixel spectral size (0.96 cm^{-1}). Then, $I_{t,c}(\nu)$ was combined with $I_0(\nu)$ to calculate instrument broadened $\alpha_{\text{CEAS}}(\nu)$. In the fifth step, the calculated $\alpha_{\text{CEAS}}(\nu)$ was iteratively compared with the measured absorbance ($-\ln(I_t(\nu)/I_0(\nu))$) using the least square method, and the temperature and OH concentration were acquired.

With the above experiment, fs-CEAS measurements were performed on LTPs with the H_2O/He and CH_4/O_2/He mixtures. Figure 2(a) first shows a representative single-shot fs-CEAS measurement on the H_2O/He plasma at the end of the 70th pulse in the burst. In Fig. 2(a), the measured fs-CEAS absorbance spectrum ($-\ln(I_t(\nu)/I_0(\nu))$) was compared against the best-fit absorbance. The laser shot-to-shot variation was corrected based on the *a priori* information that the absorbance spectrum (i.e., $-\ln(I_t(\nu)/I_0(\nu))$) portion with no absorption feature equaled zero. Before this correction, $I_0(\nu)$ was averaged over 200 shots. As seen, the best-fit absorbance was in good agreement with the measured absorbance, and the residual between them was 0.01 on average. From the fit, the temperature was inferred to be 315.7 K, while the OH mole fraction was 14.0 parts per million (ppm). Similarly, Fig. 2(b) shows another representative single-shot fs-CEAS measurement on the CH_4/O_2/He plasma at the end of a 600-discharge-pulse burst. As shown, the best-fit absorbance also agreed well with the measured absorbance with a mean residual of 0.008. The temperature and OH mole fraction extracted from this fit were determined to be 366.5 K and 11.5 ppm, respectively. Note that the spectra in Fig. 2 only displayed the absorption features of OH(X) ($v = 0$) and did not display any features of OH(X) at high vibrational levels ($v > 0$).

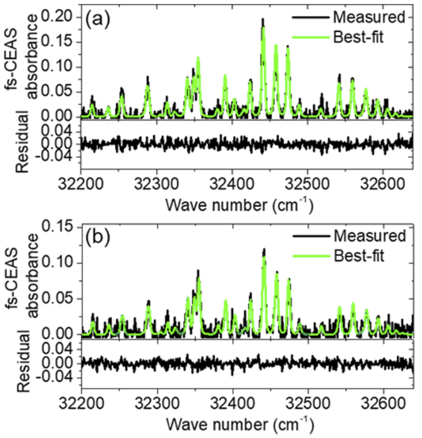

Fig. 2. Single-shot fs-CEAS measurements on (a) the H_2O/He plasma, and (b) the CH_4/O_2/He plasma.

To demonstrate the advantage of single-shot measurements offered by fs-CEAS, Fig. 3 further shows the time-dependent measurements of temperature (Fig. 3(a)) and OH concentration (Fig. 3(b)) in the repetitive ns H_2O/He plasma discharge using the single-shot fs-CEAS. These time-dependent measurements were accomplished by varying the delay time of the ns discharge pulser relative to the laser/camera, and they were separately taken at time instants 300 ns after the 50th, 55th, 60th. . . 200th discharge pulse in the burst. As seen, the measurements captured the time-dependent rise of temperature and OH in the burst discharge, providing critical validation for plasma chemistry models. Note that the error bar denoted the standard deviation of single-shot measurements taken 100 times, and it represented the total uncertainty arising both from the fs-CEAS method and the plasma reactor (e.g., discharge-to-discharge variation). The uncertainty contributed by the fs-CEAS method will be discussed below using simulations.

To quantify the superiority of fs-CEAS in detection sensitivity over past methods and reflect the quantitative nature of fs-CEAS, numerical simulations were conducted. Compared with the above experiments, simulations offered the ground truth for temperature and OH (that was difficult to be known *a priori* from experiments) along with the fs-CEAS spectrum. As a result, the OH detection sensitivity can be examined, i.e., whether fs-CEAS can infer the target parameters with acceptable accuracy at a given OH concentration. As summarized in the Supplementary material, the simulation first synthesized $I_0(\nu)$ and $I_t(\nu)$ based on the ground truth temperature and OH concentration, and then spectrally fitted the synthetic $I_0(\nu)$ and $I_t(\nu)$ to acquire temperature and OH which were compared with

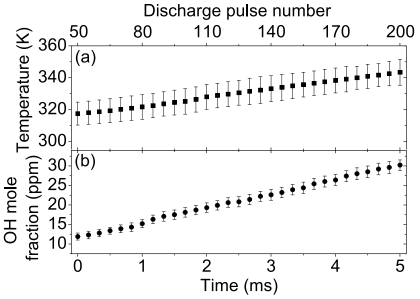

Fig. 3. Time-dependent measurements of (a) temperature and (b) OH concentration in a repetitive ns H_2O/He plasma discharge.

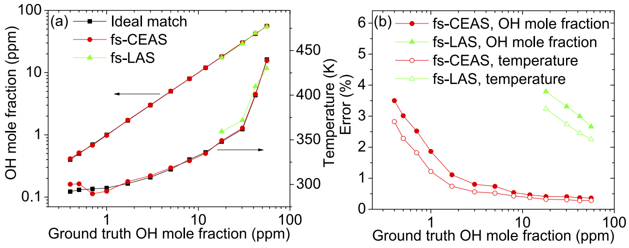

Fig. 4. (a) Comparison of fs-CEAS and fs-LAS on the OH detection sensitivity and temperature using simulations; (b) Relative errors associated with (a).

the ground truth results for examining detection sensitivity. For comparison purposes, simulations were also performed with single-pass fs laser absorption spectroscopy (fs-LAS) without any cavity enhancement with an approach similar to that of fs-CEAS.

Figure 4 shows the detection sensitivity comparison between fs-CEAS and fs-LAS using numerical simulations. Figure 4(a) shows the OH mole fractions and temperatures obtained by fs-CEAS and fs-LAS at different OH mole fractions from 0.4 (18 for fs-LAS) to 56 ppm, and Fig. 4(b) shows the OH mole fraction and temperature errors of these two methods relative to the ground truth data. Here the ground truth temperatures and OH mole fractions were obtained directly from Ref. [19] and they represented real experimental conditions of LTPs (e.g., ppm of OH radicals at 30–100 Torr and 300–600 K). The single-shot fs-CEAS was simulated when OH mole fraction was above 8 ppm, otherwise fs-CEAS was simulated with 150-shot averaging to improve the SNR. The fs-LAS was simulated with 300-shot averaging at all mole fraction levels. Both fs-CEAS and fs-LAS simulations were performed with an absorbance SNR over 5 and with error ranging from ~0.5% to ~3.5% (a typical error range of temperature and OH [20]). As shown in Figs. 4(a) and 4(b), fs-CEAS could accomplish an OH detection limit at sub-ppm level (~5×10^{11} cm^{-3} in number density) with OH mole fraction within an acceptable accuracy of 3.5% and with temperature within 2.8%. In contrast, fs-LAS could only detect OH at ~20 ppm (~1×10^{13} cm^{-3}) with accuracies of OH (within 3.8%) and temperature (within 3.2%) that were similar to those of fs-CEAS. Hence the OH detection limit was improved by ~55× by fs-CEAS compared with fs-LAS. Such ~55× improvement agreed with the theoretical prediction of ~66×, and the slight difference between them existed probably because simulations considered the real noises quantified experimentally, as detailed in the Supplementary material. Note that the error of either OH or temperature by fs-CEAS (or fs-LAS) increased with decreasing OH mole fraction, as a lower mole fraction led to a reduced SNR and a less accurate data fitting, or even failure.

In summary, this work reported fs-CEAS for sensitive, single-shot, simultaneous, and *in situ* measurements of temperature and species with ~180 ns time resolution in LTPs. Fs-CEAS was demonstrated based on the $X^2\Pi$-$A^2\Sigma^+$ transitions of OH. Fs-CEAS exhibited several benefits. Due to the optimal cavity, ~66× sensitivity enhancement was achieved, improving the actual detection limit by ~55× to the sub-ppm (10^{11} cm^{-3}) level, compared to single-pass absorption. Single-shot measurements were accomplished while retaining a ~180 ns time resolution. Due to the broadband fs laser, the cavity matched ~95 modes on each CCD pixel bandwidth over the entire 3.2 nm range (~34,000 modes in total), and therefore it became largely immune to the laser-cavity coupling noise. Also, the broadband fs laser offered many absorption features to measure multiple parameters with reduced uncertainties.

Funding. National Science Foundation (CBET-1903362, DCheM-2029425); U.S. Department of Energy (DE-SC0020233); Exxon Mobil Corporation; U.S. Department of Energy (DEFE0026825).

Disclosures. The authors declare no conflicts of interest.

Data availability. Data underlying the results presented in this paper are not publicly available at this time but may be obtained from the authors upon reasonable request.

Supplemental document. See Supplement 1 for supporting content.

REFERENCES

1. W. Sun, M. Uddi, S. H. Won, T. Ombrello, C. Carter, and Y. Ju, Combust. Flame **159**, 221 (2012).
2. Y. w. Huang, Q. f. Yu, M. Li, S. n. Sun, H. Zhao, S. x. Jin, J. Fan, and J. g. Wang, Plasma Processes Polym. **18**, 2000171 (2021).
3. M. Shenton and G. Stevens, J. Phys. D: Appl. Phys. **34**, 2761 (2001).
4. J. K. Lefkowitz, P. Guo, A. Rousso, and Y. Ju, Philos. Trans. R. Soc., A **373**, 20140333 (2015).
5. N. Popov and S. Starikovskaia, Prog. Energy Combust. Sci. **91**, 100928 (2022).
6. R. J. Tancin, Z. Chang, M. Gu, V. Radhakrishna, R. P. Lucht, and C. S. Goldenstein, Opt. Lett. **45**, 583 (2020).
7. H. U. Stauffer, P. S. Walsh, S. A. Schumaker, and S. Roy, Optica **7**, 847 (2020).
8. V. Kasyutich, C. Canosa-Mas, C. Pfrang, S. Vaughan, and R. Wayne, Appl. Phys. B **75**, 755 (2002).
9. J. T. Hodges, H. P. Layer, W. W. Miller, and G. E. Scace, Rev. Sci. Instrum. **75**, 849 (2004).
10. Z. Wang, H. Wei, Y. Li, R. Kan, and W. Ren, Opt. Lett. **45**, 1148 (2020).
11. R. J. Tancin and C. S. Goldenstein, Opt. Express **29**, 30140 (2021).
12. V. Radhakrishna, R. J. Tancin, G. Mathews, and C. S. Goldenstein, Appl. Phys. B **127**, 172 (2021).
13. T. Y. Chen, N. Liu, C. J. Kliewer, A. Dogariu, Y. Ju, and E. Kolemen, Opt. Lett. **47**, 1351 (2022).
14. S.-S. Kiwanuka, T. Laurila, J. H. Frank, A. Esposito, K. Blomberg Von Der Geest, L. Pancheri, D. Stoppa, and C. F. Kaminski, Anal. Chem. **84**, 5489 (2012).
15. A. K. Pal, N. Kumar, and R. Kshirsagar, Chem. Phys. **554**, 111420 (2022).
16. N. Liu, H. Zhong, Y. Lin, T. Y. Chen, Z. Wang, and Y. Ju, in AIAA SCITECH 2022 Forum (American Institute of Aeronautics and Astronautics, 2021), 1946.
17. N. Liu, T. Y. Chen, H. Zhong, Y. Lin, Z. Wang, and Y. Ju, Appl. Phys. Lett. **120**, 201103 (2022).
18. P. Bruggeman, G. Cunge, and N. Sadeghi, Plasma Sources Sci. Technol. **21**, 035019 (2012).
19. A. Rousso, X. Mao, Q. Chen, and Y. Ju, Proc. Combust. Inst. **37**, 5595 (2019).
20. S. Wang and R. K. Hanson, Appl. Phys. B **124**, 37 (2018).